Benchmarking the use of heavily-doped Ge for plasmonics

and sensing in the mid-infrared

Giovanni Pellegrini[†], Leonetta Baldassare[‡], Valeria Giliberti[§], Jacopo Frigerio[⊥],
Kevin Gallacher[∥], Douglas J. Paul[∥], Giovanni Isella[⊥], Michele Ortolani[‡], and
Paolo Biagioni[†,*]

[†] *Dipartimento di Fisica, Politecnico di Milano, Piazza Leonardo da Vinci 32,*
I-20133 Milano, Italy

[‡] *Dipartimento di Fisica, Sapienza Universitá di Roma, Piazzale Aldo Moro 5,*
I-00185 Rome, Italy

[§] *Center for Life Nano Sciences, Istituto Italiano di Tecnologia, Viale Regina Elena 291,*
I-00185 Rome, Italy

[⊥] *L-NESS, Dipartimento di Fisica, Politecnico di Milano, Polo di Como,*
Via Anzani 42, I-22100 Como, Italy

[∥] *School of Engineering, University of Glasgow, Rankine Building, Oakfield Avenue,*
*Glasgow G12 8LT, United Kingdom*

E-mail: paolo.biagioni@polimi.it

Keywords: plasmonics, mid-infrared, sensing, germanium, heavy-doping

Abstract

Despite the recent introduction of heavily-doped semiconductors for mid-infrared plasmonics, it still remains an open issue whether such materials can compete with noble metals. A whole set of figures of merit are employed to thoroughly assess the use of heavily-doped Ge on Si as a mid-infrared plasmonic material and benchmark it against standard noble metals such as Au. A full-wave electrodynamics framework is used to model and design high-performance, silicon-foundry compatible mid-infrared plasmonic sensors based on experimental material data reaching plasma wavelengths down to $\lambda_p \sim 3.1$ μm. It is finally shown that Ge sensors can provide signal enhancements for vibrational spectroscopy above the 3 orders of magnitude, thus representing a promising alternative to noble metals, leveraging the full compatibility with the silicon foundry microfabrication processes.

TOC Graphic

Decreasing Ge
Plasma Frequency

Increasing
Ge Doping
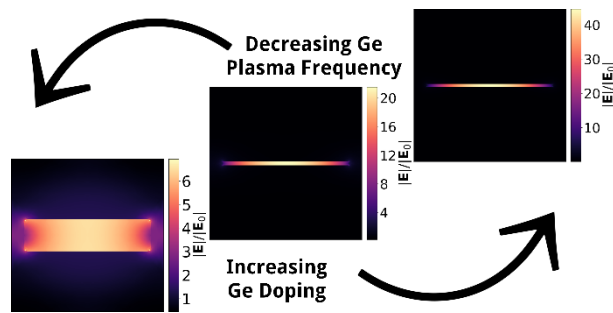
Over the last ten years, heavily-doped semiconductors have entered the field of mid-infrared (mid-IR) and THz plasmonics as a promising alternative to standard metals.[1–14] While Au, Ag, and Al (the materials typically employed in the visible and near-IR) have a plasma frequency in the near-UV and therefore behave as very good conductors in the mid-IR range, heavily-doped semiconductors possess a much lower plasma frequency (here defined as the frequency where the real part of the permittivity is zero) by virtue of their lower carrier density, which typically reaches values up to the order of $n \sim 10^{19}$-10^{20} cm^{-3}. For this reason, heavily-doped semiconductors, when compared to metals in the mid-IR, are characterized by a much lower absolute value of the negative real part of the dielectric function $\varepsilon = \varepsilon_1 + i\varepsilon_2$, a feature that can be seen as the essence of the difference between a 'metallic' and a 'plasmonic' material.

To this extent, indeed, heavily-doped semiconductors behave in the mid-IR as much as standard noble metals behave in the visible, i.e. the region that represented the core spectral window for plasmonic applications so far. This has already been discussed in the literature also by stressing the fact that for several mid-IR applications, such as e.g. epsilon-near-zero phenomena and metamaterials, a truly 'plasmonic' material (which we might arbitrarily define as a material with $-50 < \varepsilon_1 < 0$) is needed.[5]

With such values of ε_1, which are e.g. typical of Au in the visible spectrum, the skin depth for the field penetration inside the material is not negligible compared to the wavelength, an occurrence that is accompanied by the presence of volume currents and therefore larger losses.[15] Typically, therefore, properly tuned metal nanostructures (referred to as 'nanoantennas') are employed to compensate for the losses by creating resonantly enhanced near fields.[16,17] Besides the local intensity enhancement, the most prominent feature that characterizes a 'plasmonic' material, as opposed to a 'metallic' one is, however, the intrinsic ability to confine such local fields over a strongly sub-diffraction length. This has been already exploited for decades in sensing applications at visible wavelengths, such as those based on a flat gold film sustaining

surface plasmon polaritons (SPPs). In these applications, the strong field confinement increases the sensitivity to local changes in the refractive index and allows very low molecular concentrations to be addressed. From this point of view, the difference between a 'metallic' and a 'plasmonic' surface is readily understood when the SPP decay length δ towards the vacuum half-space is considered. As a meaningful example for the mid-IR spectral region, in the case of Au at $\lambda \sim 12$ µm we typically have $\varepsilon_{1,Au} \sim -1000$ and we obtain a decay constant towards the vacuum $\delta_{Au} \sim 147$ µm, which is a clear indication that such surface waves are very weakly confined and, with a dispersion relation that is extremely close to the light cone, cannot be properly regarded as SPPs. For heavily-doped Ge, on the other side, with doping densities ranging from $n \sim 2.5 \; 10^{19}$ cm^{-3} to $n \sim 2.1 \; 10^{20}$ cm^{-3} we find a real part of $\varepsilon_{1,Ge}$ ranging from about -6 to about -200, as discussed later on in this work, and a decay length ranging from $\delta_{Ge} \sim 5$ µm to $\delta_{Ge} \sim 30$ µm at the same operating wavelength. This comparison illustrates the larger field confinement provided by the heavily-doped Ge, which nevertheless comes at the expenses of a shorter propagation length, as expected because of the larger losses that unavoidably accompany the confinement, as also stressed in some recent analyses of semiconductor plasmonics.[19,20]

In the mid-IR, plasmonic antennas have been employed over the last few years as a means to boost vibrational spectroscopies that address the fingerprint vibrational features of specific molecules (surface-enhanced IR absorption, SEIRA), with key applications in biology, medicine, and security.[5,7,8,21-32] When nanoparticles, and especially narrow gaps between coupled nanoparticles, are employed, the high degree of field confinement is largely granted by the boundary conditions set by the particle geometry rather than by the material properties themselves and the distinction made above between 'plasmonic' and 'metallic' behaviors can become less relevant. Indeed, gold gap nanoantennas with record enhancement values of the IR vibrational absorption signal exceeding four orders of magnitude have been demonstrated.[26,27]

Semiconductors (especially group-IV semiconductors), however, still have unique properties in terms of material quality, tunability, and compatibility with the current microelectronic industry. It is, therefore, essential to benchmark the performance of heavily-doped mid-IR nanoantennas against that of metal nanoantennas in order to assess their potential as novel sensing platforms.

In this paper we first employ an analysis tool introduced recently by Dastmalchi *et al.*[33] that allows for a direct assessment of the trade-off between losses and field confinement in SPPs supported at the interface between vacuum and different plasmonic materials. We exploit this approach to directly compare the mid-IR performance of Au and of heavily-doped Ge epitaxially grown on Si wafers by means of low-energy plasma-enhanced chemical vapor deposition.[18,34] We then introduce a set of figures of merit to assess, by full electrodynamics simulation, the performance of a plasmonic sensing platform made of n-type Ge, focusing our attention on slit arrays that have been demonstrated to outperform standard dipolar antennas.[28] This thorough analysis allows for a better understanding of the differences between metals and heavily-doped semiconductors in the mid-IR and confirms that semiconductors indeed represent a promising alternative for sensing applications.

Results and Discussion

Material Optical Properties

The representation introduced by Dastmalchi *et al.* plots the dielectric constant of different materials in a reference frame where the two axis display figures of merit (FOMs) for the field confinement and the propagation length of SPPs.[33] The two FOMs are calculated starting from the complex wavevector components $k_{\parallel}$ and $k_{\perp}$ that determine the modulus of the SPP wave vector $\mathbf{k}_{SPP}$ at a flat metal-vacuum interface. One can define a FOM for the characteristic SPP propagation length (which is directly related to losses) as $FOM_{Prop} = k_{spp}/2\pi\mathrm{Im}(k_{\parallel})$ and one for the field confinement toward the vacuum half-space as $FOM_{Conf} = \lambda\,\mathrm{Im}(k_{\perp})$. We use experimentally-retrieved dielectric functions of heavily-doped Ge and Au to calculate the propagation and confinement figures of merit.[10,18,35,36] The heavily-doped Ge is obtained by a high incorporation of P dopants during the growth, followed by an annealing step to activate the dopant atoms. The process leads to an activated carrier concentration ranging from $n \sim 2.5\times10^{19}$ cm^{-3} to $n \sim 2.1\times10^{20}$ cm^{-3}, with corresponding plasma wavelengths reaching $\lambda_{p} \sim 3.1$ µm. The experimental dielectric functions are characterized by means of Fourier-transform IR spectroscopy and extracted through the combined use of Drude-Lorentz modelling and Kramers-Kronig relations.[10] For the present analysis, we shall use three different heavily-doped Ge materials labeled as 9338, 9547 and 10258:[10,18,35] all the relevant optical and electrical parameters are reported in **Table 1**. The specific choice of these three samples is motivated by the fact that the respective doping levels allow the whole mid-infrared region to be covered and therefore these samples fully demonstrate the versatility and tunability of the proposed material platform. Moreover, they have all been experimentally demonstrated and characterized previously, thus allowing the present analysis to develop from a solid basis.

The dielectric functions displayed in **Figure 1a** confirm that a proper tailoring of the Ge doping level allows for a continuous tuning of the plasma wavelength over almost the whole mid-IR

Table 1: Material and geometrical parameters for SEIRA sensing platforms: carrier concentration (n), plasma wavelength (λ_p), slit length (L), slit width(w) and square unit cell size. (Δ), DC mobility (μ), and effective mass (m*).

	n (cm^{-3})	λ_p (μm)	L (nm)	w (nm)	Δ (nm)	μ (cm^2/Vs)	m*
Ge 9338	$2.5 \cdot 10^{19}$	10.0	200	50	240	300	0.12
Ge 9547	$8.8 \cdot 10^{19}$	5.6	1500	50	1800	98	0.12
Ge 10258	$2.1 \cdot 10^{20}$	3.1	2500	50	3000	76	0.12
Au	//	//	4000	50	4800	//	//

range. Furthermore, we observe that for all the Ge samples the real part of the dielectric function ε_1 reaches values down to, at most, $\varepsilon_{Ge,1} \sim -100$, while in the case of Au we notice that ε_1 drops to $\varepsilon_{Au,1} \sim -10^4$ at lower energies, highlighting its nature of almost perfect conductor in this wavelength range. When inspecting **Figure 1b**, which compares the Ge 9547 sample ($\lambda_p \sim 5.6$ μm) to Au, we can see that the latter, being a very good conductor in the mid-IR, is subject to much lower losses (larger FOM_{Prop}) because of the smaller penetration depth of the electromagnetic field inside the metal. This happens in spite of the larger imaginary part of the optical constant, which therefore cannot be taken as a direct indication to assess the quality of the plasmonic resonances in this wavelength range, as already discussed in a recent publication.[20] On the other hand, Au is also characterized by a significantly worse field confinement (lower FOM_{Conf}), with Ge outperforming Au by about one order of magnitude. We can carry out a similar comparison between the three heavily-doped Ge samples, as reported in **Figure 1c**. A first cursory glance reveals that the three materials are roughly similar in terms of confinement and propagation properties, nevertheless a closer look shows that the largely different plasma wavelengths lead to extremely distinct confinement and propagation FOMs if
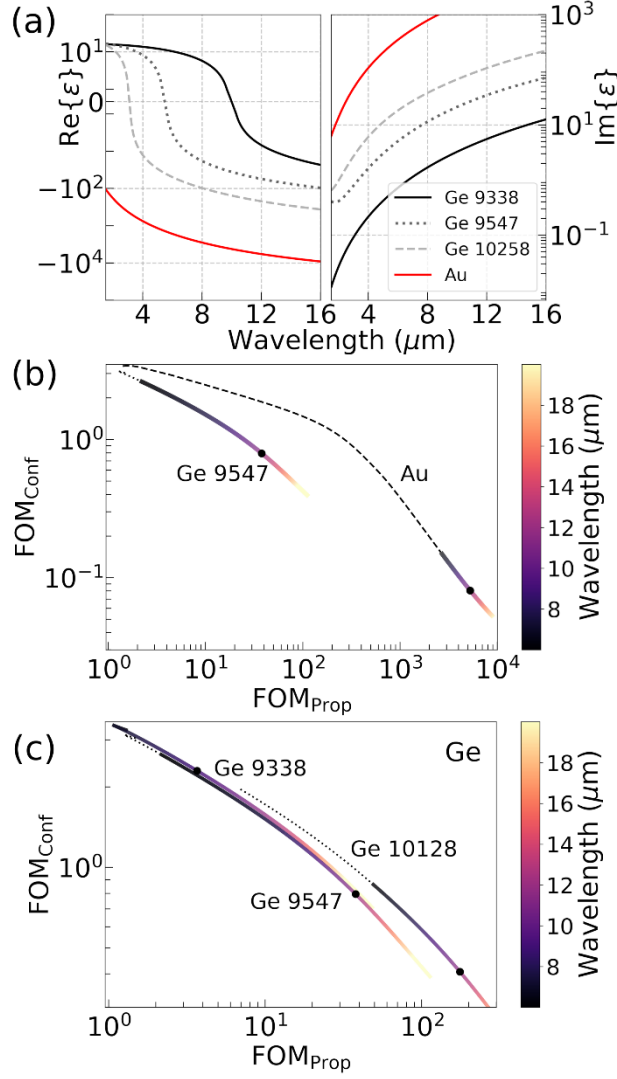
Figure 1: (a) Real and Imaginary part of heavily-doped Ge and Au dielectric functions. (b) Representation of the confinement and propagation length of heavily-doped Ge 9547 and Au.[18,33,36] (c) Representation of the confinement and propagation lengths for the three chosen heavily-doped Ge materials (9338, 9547 and 10258):[10,18,35] the black dots indicate the $\lambda \sim 12$ μm wavelength.

we compare the materials at a fixed working wavelength. As an example, the difference in FOM_{prop} between the 9338 ($\lambda_p \sim 10.0$ μm) and 10258 ($\lambda_p \sim 3.1$ μm) materials can be as large as two orders of magnitude at $\lambda \sim 12$ μm. This wide range of tunability of the plasmonic response is a peculiar feature of heavily-doped semiconductors with no counterparts in standard metals and allows for the fine tuning of the intrinsic infrared material response to meet the requirements of each specific application.
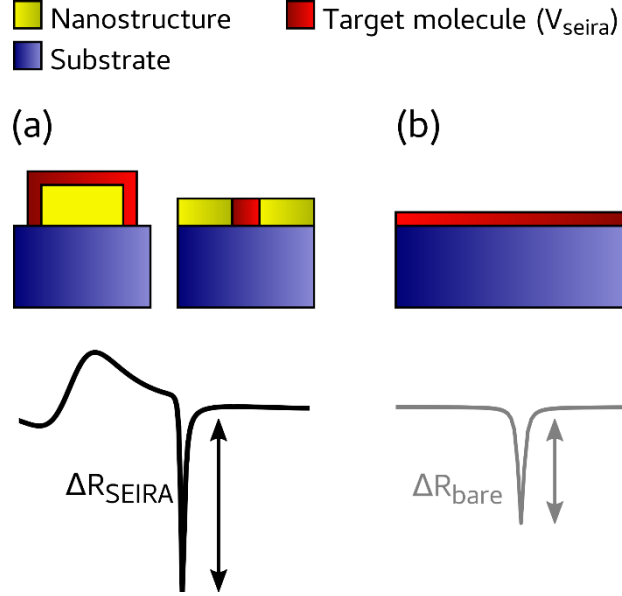
Figure 2: (a) Schematic representation of nanoantenna and nanoslit SEIRA sensing platforms and of the corresponding baseline-corrected reflectance SEIRA signal (ΔR_{SEIRA}). (b) Reference reflectance signal for the same volume V_{SEIRA} of target molecules deposited on the bare substrate (ΔR_{bare}).

Sensing Figures of Merit

We now introduce three different metrics to estimate the performance of SEIRA plasmonic platforms and directly compare heavily-doped Ge and Au by considering an actual sensing application. The metrics are defined as a function of two quantities determined in a far-field reflection geometry. The first one is defined as ΔR_{SEIRA} and corresponds to the baseline-corrected surface-enhanced SEIRA signal of a volume V_{SEIRA} of target molecules interacting with the Ge-on-Si plasmonic platform (**Figure 2a**). The second quantity is instead defined as ΔR_{bare} and coincides with the vibrational signal arising from the same volume V_{SEIRA} deposited on a bare Si substrate (**Figure 2b**).

In this framework the first introduced figure of merit is simply defined as $FOM_{\text{SNR}} = \Delta R_{\text{SEIRA}}$. This serves as a proxy of the measured signal intensity and allows the monitoring of the platform signal-to-noise ratio that is directly proportional to ΔR_{SEIRA}.

The second proposed metric is defined as the ratio of the baseline-corrected SEIRA signal amplitude to the one of the bare target molecule, i.e. $FOM_{\text{SEIRA}} = \Delta R_{\text{SEIRA}}/\Delta R_{\text{bare}}$. This metric monitors the SEIRA enhancement performance and, for a selected vibrational line of a given
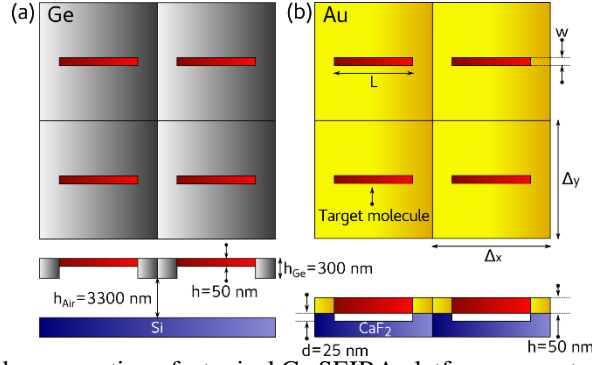
10

Figure 3: (a) Top view and cross section of a typical Ge SEIRA platform geometry. Target molecules fill only the top 50 nm of the slit volume to model realistic wetting conditions and to allow for a straightforward comparison with the Au platform. (b) Top view and cross section of a typical Au SEIRA platform geometry. Target molecules are shown in red and completely fill the Au nanoslit.

target molecule, it is solely related to the intrinsic signal enhancement properties of the sensing device. It is therefore an ideal benchmark to compare platforms characterized by different geometries and different employed plasmonic or metallic materials, providing a straightforward guideline for an efficient design of SEIRA sensing nanostructures.

The last considered metric aims at the description of the measured SEIRA signal in a realistic experimental setup. In these conditions, a volume $V_{\text{tot}} = V_{\text{SEIRA}} + V_{\text{uncoupled}}$ of analyte is usually present on the sensing platform, where only a limited volume (V_{SEIRA}) of the target molecules interacts with the plasmonic nanostructure, while the remaining volume fraction ($V_{\text{uncoupled}}$) experiences no significant signal enhancement. In order to track the signal enhancement between the sensing platform and the same molecules deposited onto a reference substrate, starting from the quantities ΔR_{SEIRA} and ΔR_{bare}, it is then necessary to consider a normalization coefficient including the relative volume fraction of the sensitized molecules, finally obtaining:

$$FOM_{\text{exp}} = \left(\frac{\Delta R_{\text{SEIRA}}}{\Delta R_{\text{bare}}}\right)\left(\frac{V_{\text{SEIRA}}}{V_{\text{uncoupled}}}\right). \tag{1}$$

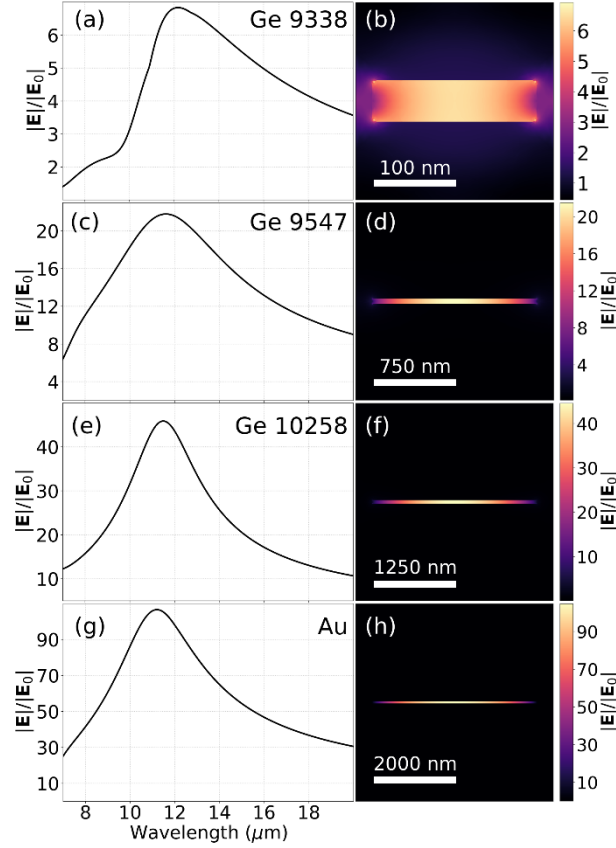**Figure 4:** Local field spectra and in-plane resonant maps for the heavily-doped Ge and Au SEIRA sensing platform operating at $\lambda \sim 12$ μm: (a,b) Ge 9338 ($\lambda_\mathrm{p} \sim 10$ μm, width 50 nm, length 200 nm), (b,c) Ge 9547 ($\lambda_\mathrm{p} \sim 5.6$ μm, width 50 nm, length 1500 nm), (e,f) Ge 10258 ($\lambda_\mathrm{p} \sim 3.1$ μm, width 50 nm, length 2500 nm), (g,h) Au (width 50 nm, length 4000 nm).

The combined use of the three proposed quantities allows one to take all possible design requirements and experimental occurrences into account, capturing different aspects of plasmon-enhanced sensing.

Mid-Infrared Sensing Platforms: Design and Performance

As a practical example, we employ the three figures of merit introduced above to compare, using a multilayer finite-element method approach,[37] the performance of Ge-based sensing devices with those of Au-based, state-of-the-art SEIRA platforms. The Ge device consists of a free-standing, 300 nm-thick Ge membrane patterned with a fully etched nanoslit array and suspended 3300 nm above a Si substrate. The suspended membrane design is introduced to decouple the plasmonic material from the highly polarizable Si substrate, with the air gap width

chosen to obtain constructive interference with the light reflected at the Si interface.[38] The geometrical parameters of the slit and the unit cell, reported in Table 1, are tuned to obtain a resonant system at $\lambda \sim 12$ μm for each of the three heavily-doped Ge materials (**Figure 3a**). The Au SEIRA platform consists of an Au nanoslit array deposited on a CaF$_2$ substrate.[28] Also in this case, the slit width and length and the unit cell stride, reported in **Table 1**, are chosen to obtain a resonant system at $\lambda \sim 12$ μm, while the depth is $h = 50$ nm, with an additional $d = 25$ nm overetching into the CaF$_2$ substrate to further increase the field enhancement and match the design already proposed in the literature (**Figure 3b**).[28] It is worth noting that the free-standing Ge membrane design is well within the nanofabrication capabilities of group-IV technologies and therefore fully leverages the compatibility with the Si technological platform. The same approach is not needed for the Au array, given the lower refractive index of the CaF$_2$ substrate, and anyway would represent a significant challenge from the fabrication standpoint, even if free-standing hybrid metallic gratings have been obtained by evaporating Au on suspended SiN nanostructured membranes.[39]

In this simulation framework the target molecules are described by means of a single Lorentzian oscillator, whose frequency-dependent dielectric function can be described as:

$$\varepsilon_{\text{molecule}} = 1 + \frac{\Omega}{\omega_0^2 - \omega^2 - i\gamma\omega}. \tag{2}$$

We choose an oscillator strength $\Omega = 90$ cm^{-1}, a damping constant $\gamma = 10$ cm^{-1}, and an oscillation frequency $\omega_0 = 845$ cm^{-1} ($\lambda \sim 12$ μm), to work in an energy range that is fully representative of the fingerprint spectral region and that has e.g. been recently assigned to DNA sugar ring vibrations.[40]

Figure 4 reports the local field enhancement spectra and the in-plane maps for all the Ge and the Au sensing platforms, where the field maps are taken at the top-end of the slit cross-section. All the Ge platforms resonate around $\lambda \sim 12$ μm and differ greatly in terms of peak field values
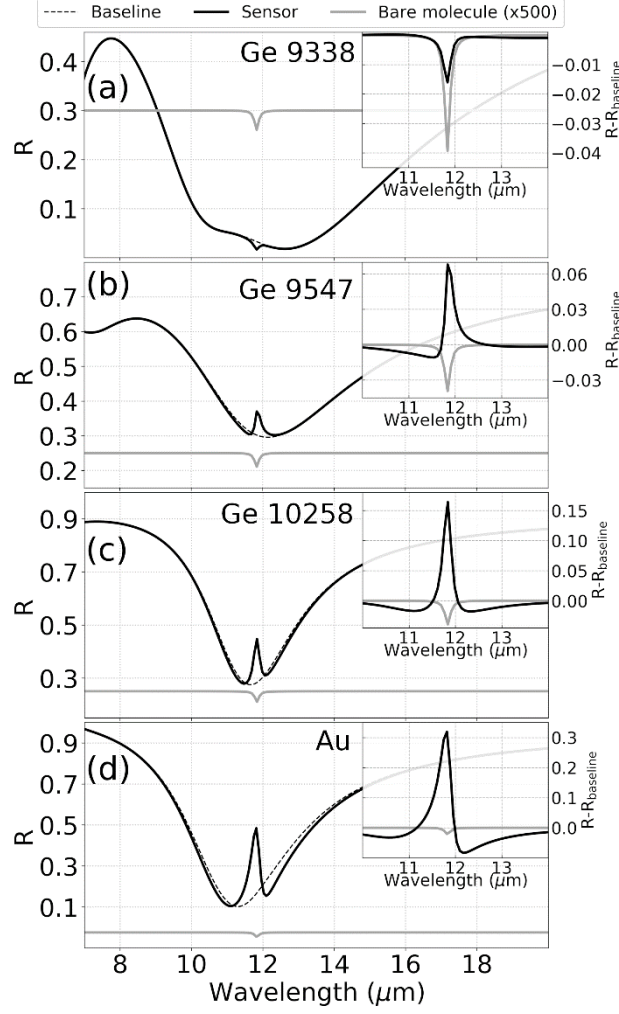
Figure 5: Reflectance and baseline corrected SEIRA vibrational signals (insets) for the heavily-doped Ge and Au SEIRA sensing platform operating at $\lambda\sim12$ µm. : (a) Ge 9338 ($\lambda_p\sim10$ µm), (b) Ge 9547 ($\lambda_p\sim5.6$ µm), (c) Ge 10258 ($\lambda_p\sim3.1$ µm), (d) Au.

and spectral line shape of the resonance. The maximum field enhancement increases monotonically with the doping from the 9338 to the 10258 Ge sample, reaching values of up to $|\mathbf{E}|/|\mathbf{E_0}| \sim 45$ in the case of the largest Ge carrier density ($n \sim 2.1\times10^{20}$ cm^{-3}) and correspondingly lowest plasma wavelength ($\lambda_p \sim 3.1$ µm). Likewise, the narrow resonance displayed by the 10258 sample reveals the role of the reduced optical losses in reaching the best field enhancements. It is equally interesting to note the strongly asymmetric spectral shape displayed by the 9338 Ge sample, where the sharp drop on the high energy side of the spectrum can be attributed to the presence of the Ge 9338 plasma edge. The Au nanoslit geometry (**Figure 4g,**h) is nevertheless capable of even higher field enhancements, reaching values twice

14

Table 2: Figures of merit for heavily-doped Ge sensing devices and reference, state-of-the-art Au SEIRA platforms.

	FOM$_{SNR}$	FOM$_{SEIRA}$	FOM$_{exp}$
Ge 9338	0.01	$2.5 \cdot 10^1$	$0.47 \cdot 10^1$
Ge 9547	0.08	$1.2 \cdot 10^3$	$2.7 \cdot 10^1$
Ge 10258	0.14	$3.7 \cdot 10^3$	$5.2 \cdot 10^1$
Au	0.42	$2.1 \cdot 10^4$	$2.0 \cdot 10^2$

as large if compared with the best performing Ge platform, up to $|\mathbf{E}|/|\mathbf{E}_0| \sim 90$. It should also be noted that the geometry displayed in **Figure 4b** features a horizontal pitch that does not completely rule out near-field coupling between adjacent slits. However, we verified by additional simulations that this affects the local field enhancement in the slit by no more than 10%.

In order to gauge the platform sensing performance in a realistic scenario, we model the raw and baseline corrected SEIRA spectra for all the sensing platforms, as reported in **Figure 5**. In the case of the Ge sensing setup we only fill the top 50 nm of the 300 nm deep slit to provide a fair comparison with the thinner Au device and also to reproduce a possibly realistic wetting scenario, while for the Au device the whole slit is filled. All the reflectance spectra display a broad minimum in correspondence with the local field resonance, along with the vibrational signature of the target molecule observable as a marked feature superimposed to the smooth spectral profile of the slit resonance. The interaction between the Ge 9338 platform and the target molecule (**Figure 5a**) appears as an additional spike on the smooth reflection profile: this peculiar behavior can be interpreted as the signature of a weaker coupling process dominated by absorption.[30] In all the remaining setups the molecule-slit interaction emerges as a pronounced dip in the reflection profile, with larger signals in correspondence of higher field

enhancements. We frame these results in terms of the figures of merit introduced above, and resume them in **Table 2**. The emerging picture confirms that the adoption of Au always leads to the best performing sensing platform, as already suggested in the recent literature.[20] Nevertheless, the Ge 10258 device achieves values as high as $FOM_{SNR} \sim 0.15$, with raw enhancements well above the 3 orders of magnitude ($FOM_{SEIRA} \sim 4 \times 10^3$) and 50-fold signal enhancement in a realistic experimental setup ($FOM_{exp} \sim 50$). Regardless of the adopted metric, the Ge sensing performance is at most 3 to 5 times worse than the noble metal counterpart, while featuring all the advantages mentioned above in terms of material quality, tunability, and silicon-foundry process compatibility, which for many applications might represent the only viable route toward fabrication.

It is finally interesting to investigate the sensor performance as a function of the unit cell aspect ratio, keeping all the geometrical parameters fixed apart from Δy. An analysis of the data displayed in **Figure 6** returns a picture consistent with the results presented in **Table 2** but provides further insight into the sensing platform behavior. Unsurprisingly, the Au based devices display the best performance along the whole parametric sweep, while the best Ge-based platform is always the one fabricated from the 10258 material. Elongated elementary cells ($\Delta y > \Delta x$) lead to better single cell performance (better FOM_{SEIRA}), a behavior that can be
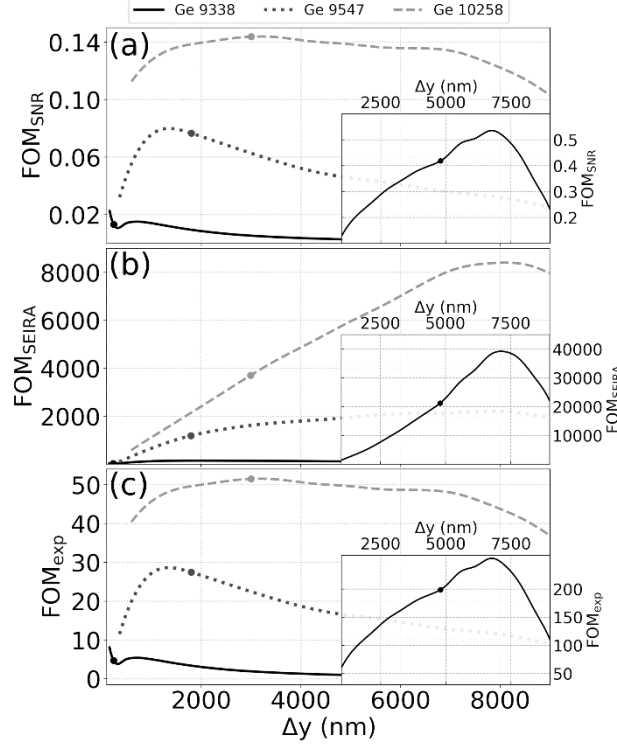
16

Figure 6: (a) Figure of merit FOM_{SNR} for the three heavily-doped Ge sensing platforms as a function of the cell parameter Δy. The dots highlight the square cell. Inset: FOM_{SNR} for the Au sensing platform. (b) FOM_{SEIRA} (c) FOM_{exp}.

readily explained in terms of constructing interference between surface plasmons traveling at the doped semiconductor interfaces.[28] The same effect is less pronounced for the FOM_{SNR} and FOM_{exp} figures of merit, since the stronger enhancements are mitigated by the smaller relative sensing active area in a larger unit cell (**Figure 6a,c**). A remarkable closing observation is that the FOM_{SNR} and FOM_{exp} line shapes are identical down to a proportionality constant. This offers a clear indication that the raw reflectance molecular signal (ΔR_{SEIRA}, FOM_{SNR}) can be expressed as the enhancement of a single slit (FOM_{SEIRA}) multiplied by the fraction of molecules located in the sensing volume.

Conclusions

In conclusion, the present modeling efforts, along with the introduced metrics, allow for a fair comparison between heavily-doped Ge-based sensing devices, based on state-of-the-art epitaxial material growth and silicon foundry technology, and Au SEIRA platforms. In the

17

appropriate energy regimes, Ge-based sensing platforms do not outperform Au-based devices, but exhibit enhancement values almost comparable with those obtained with noble metal plasmonic nanostructures, reaching signal enhancements above 3 orders of magnitude. While III-V semiconductor alloys[5,6,8] have also been proposed for mid-infrared plasmonics, with the possible advantage of a smaller effective mass for the conduction electrons (allowing for higher plasma frequencies at a given doping level), such materials lack full compatibility with the silicon foundry processes. Therefore, sensing platforms based on heavily-doped Ge represent a viable candidate for the fabrication of high-quality, integrated silicon-compatible SEIRA devices operating in the mid-IR range.

References

(1) West, P. r.; Ishii, S.; Naik, G. v.; Emani, N. k.; Shalaev, V. m.; Boltasseva, A. Searching for Better Plasmonic Materials. *Laser Photonics Rev.* **2010**, *4* (6), 795–808.

(2) Shahzad, M.; Medhi, G.; Peale, R. E.; Buchwald, W. R.; Cleary, J. W.; Soref, R.; Boreman, G. D.; Edwards, O. Infrared Surface Plasmons on Heavily Doped Silicon. *J. Appl. Phys.* **2011**, *110* (12), 123105.

(3) Boltasseva, A.; Atwater, H. A. Low-Loss Plasmonic Metamaterials. *Science* **2011**, *331* (6015), 290–291.

(4) Ginn, J. C.; Jarecki, R. L.; Shaner, E. A.; Davids, P. S. Infrared Plasmons on Heavily-Doped Silicon. *J. Appl. Phys.* **2011**, *110* (4), 043110.

(5) Law, S.; Yu, L.; Rosenberg, A.; Wasserman, D. All-Semiconductor Plasmonic Nanoantennas for Infrared Sensing. *Nano Lett.* **2013**, *13* (9), 4569–4574.

(6) Law, S.; Roberts, C.; Kilpatrick, T.; Yu, L.; Ribaudo, T.; Shaner, E. A.; Podolskiy, V.; Wasserman, D. All-Semiconductor Negative-Index Plasmonic Absorbers. *Phys. Rev. Lett.* **2014**, *112* (1), 017401.

(7) Baldassarre, L.; Sakat, E.; Frigerio, J.; Samarelli, A.; Gallacher, K.; Calandrini, E.; Isella, G.; Paul, D. J.; Ortolani, M.; Biagioni, P. Midinfrared Plasmon-Enhanced Spectroscopy with Germanium Antennas on Silicon Substrates. *Nano Lett.* **2015**, *15* (11), 7225–7231.

(8) Barho, F. B.; Gonzalez-Posada, F.; Milla-Rodrigo, M.-J.; Bomers, M.; Cerutti, L.; Taliercio, T. All-Semiconductor Plasmonic Gratings for Biosensing Applications in the Mid-Infrared Spectral Range. *Opt. Express* **2016**, *24* (14), 16175–16190.

(9) Fischer, M. P.; Schmidt, C.; Sakat, E.; Stock, J.; Samarelli, A.; Frigerio, J.; Ortolani, M.; Paul, D. J.; Isella, G.; Leitenstorfer, A.; et al. Optical Activation of Germanium Plasmonic Antennas in the Mid-Infrared. *Phys. Rev. Lett.* **2016**, *117* (4), 047401.

(10) Frigerio, J.; Ballabio, A.; Isella, G.; Sakat, E.; Pellegrini, G.; Biagioni, P.; Bollani, M.; Napolitani, E.; Manganelli, C.; Virgilio, M.; et al. Tunability of the Dielectric Function

of Heavily Doped Germanium Thin Films for Mid-Infrared Plasmonics. *Phys. Rev. B* **2016**, *94* (8), 085202.

(11) Gómez Rivas, J.; Schotsch, C.; Haring Bolivar, P.; Kurz, H. Enhanced transmission of THz radiation through subwavelength holes. *Phys. Rev. B* **2003**, *68*, 201306(R).

(12) Giannini, V.; Berrier, A.; Maier, S. A.; Sánchez-GIl, J. A.; Gómez Rivas, J. Scattering efficiency and near field enhanceemnt of active semicondutor plasmonic antennas at terahertz frequencies. *Opt. Exp.* **2010**, *18*(3), 2797.

(13) Berrier, A.; Albella, P.; Ameen Poyli, M.; Ulbricht, R.; Bonn, M.; Aizpurua, J.; Gómez Rivas, J. Detection of deep-subwavelength dielectric layers at terahertz frequencies using semiconductor plasmonic resonators. *Opt. Exp.* **2012**, *20*(5), 5052.

(14) Law, S.; Podolskiy, V.; Wasserman, D. Towards nano-scale photonics with micro-scale photons: the opportunities and challenges of mid-infrared plasmonics. *Nanophotonics* **2013**, *2*, 103–130.

(15) Dorfmüller, J.; Vogelgesang, R.; Khunsin, W.; Rockstuhl, C.; Etrich, C.; Kern, K. Plasmonic Nanowire Antennas: Experiment, Simulation, and Theory. *Nano Lett.* **2010**, *10* (9), 3596–3603.

(16) Novotny, L.; van Hulst, N. Antennas for Light. *Nat Photon* **2011**, *5* (2), 83–90.

(17) Biagioni, P.; Huang, J.-S.; Hecht, B. Nanoantennas for Visible and Infrared Radiation. *Rep. Prog. Phys.* **2012**, *75* (2), 024402.

(18) Frigerio, J.; Ballabio, A.; Gallacher, K.; Gilberti, V.; Baldassarre, L.; Millar, R.; Milazzo, R.; Maiolo, L.; Minotti, A.; F Bottegoni; et al. Optical Properties of Highly N-Doped Germanium Obtained by in Situ Doping and Laser Annealing. *J. Phys. Appl. Phys.* **2017**, *50* (46), 465103.

(19) Khurgin, J. B. Replacing Noble Metals with Alternative Materials in Plasmonics and Metamaterials: How Good an Idea? *Phil Trans R Soc A* **2017**, *375* (2090), 20160068.

(20) Hsieh, W. T.; Wu, P. C.; Khurgin, J. B.; Tsai, D. P.; Liu, N.; Sun, G. Comparative Analysis of Metals and Alternative Infrared Plasmonic Materials. *ACS Photonics* **2017**.

(21) Neubrech, F.; Pucci, A.; Cornelius, T. W.; Karim, S.; García-Etxarri, A.; Aizpurua, J. Resonant Plasmonic and Vibrational Coupling in a Tailored Nanoantenna for Infrared Detection. *Phys. Rev. Lett.* **2008**, *101* (15), 157403.

(22) Neubrech, F.; Weber, D.; Katzmann, J.; Huck, C.; Toma, A.; Di Fabrizio, E.; Pucci, A.; Härtling, T. Infrared Optical Properties of Nanoantenna Dimers with Photochemically Narrowed Gaps in the 5 Nm Regime. *ACS Nano* **2012**, *6* (8), 7326–7332.

(23) Adato, R.; Yanik, A. A.; Amsden, J. J.; Kaplan, D. L.; Omenetto, F. G.; Hong, M. K.; Erramilli, S.; Altug, H. Ultra-sensitive vibrational spectroscopy of protein monolayers with plasmonic nanoantenna arrays. *P. Natl. Acad. Sci. USA* **2009**, *106*, 19227-19232.

(24) Adato, R.; Altug, H. In-Situ Ultra-Sensitive Infrared Absorption Spectroscopy of Biomolecule Interactions in Real Time with Plasmonic Nanoantennas. *Nat. Commun.* **2013**, *4*, 2154.

(25) Adato, R.; Artar, A.; Erramilli, S.; Altug, H. Engineered Absorption Enhancement and Induced Transparency in Coupled Molecular and Plasmonic Resonator Systems. *Nano Lett.* **2013**, *13* (6), 2584–2591.

(26) Brown, L. V.; Zhao, K.; King, N.; Sobhani, H.; Nordlander, P.; Halas, N. J. Surface-Enhanced Infrared Absorption Using Individual Cross Antennas Tailored to Chemical Moieties. *J. Am. Chem. Soc.* **2013**, *135* (9), 3688–3695.

(27) Brown, L. V.; Yang, X.; Zhao, K.; Zheng, B. Y.; Nordlander, P.; Halas, N. J. Fan-Shaped Gold Nanoantennas above Reflective Substrates for Surface-Enhanced Infrared Absorption (SEIRA). *Nano Lett.* **2015**, *15* (2), 1272–1280.

(28) Huck, C.; Vogt, J.; Sendner, M.; Hengstler, D.; Neubrech, F.; Pucci, A. Plasmonic Enhancement of Infrared Vibrational Signals: Nanoslits versus Nanorods. *ACS Photonics* **2015**, 1489–1497.

(29) Limaj, O.; Etezadi, D.; Wittenberg, N. J.; Rodrigo, D.; Yoo, D.; Oh, S.-H.; Altug, H. Infrared Plasmonic Biosensor for Real-Time and Label-Free Monitoring of Lipid Membranes. *Nano Lett.* **2016**, *16* (2), 1502–1508.

(30) Neuman, T.; Huck, C.; Vogt, J.; Neubrech, F.; Hillenbrand, R.; Aizpurua, J.; Pucci, A. Importance of Plasmonic Scattering for an Optimal Enhancement of Vibrational Absorption in SEIRA with Linear Metallic Antennas. *J. Phys. Chem. C* **2015**, *119* (47), 26652–26662.

(31) Neubrech, F.; Huck, C.; Weber, K.; Pucci, A.; Giessen, H. Surface-enhanced infrared spectroscopy using resonant nanoantennas. *Chem. Rev.* **2017**, 117, 5110–5145.

(32) Mayerhöfer, T. G.; Popp, J. Periodic array-based substrates for surface-enhanced infrared spectroscopy. *Nanophotonics* **2018**, *7*, 39–79.

(33) Dastmalchi, B.; Tassin, P.; Koschny, T.; Soukoulis, C. M. A New Perspective on Plasmonics: Confinement and Propagation Length of Surface Plasmons for Different Materials and Geometries. *Adv. Opt. Mater.* **2016**, *4* (1), 177–184.

(34) Isella, G.; Chrastina, D.; Rössner, B.; Hackbarth, T.; Herzog, H.-J.; König, U.; von Känel, H. Low-Energy Plasma-Enhanced Chemical Vapor Deposition for Strained Si and Ge Heterostructures and Devices. *Solid-State Electron.* **2004**, *48* (8), 1317–1323.

(35) Paul, D. J.; Gallacher, K.; Millar, R. W.; Giliberti, V.; Calandrini, E.; Baldassarre, L.; Fischer, M. P.; Frigerio, J.; Ballabio, A.; Sakat, E.; et al. N-Ge on Si for Mid-Infrared Plasmonic Sensors. In *2017 IEEE Photonics Society Summer Topical Meeting Series (SUM)*; 2017; pp 125–126.

(36) Olmon, R. L.; Slovick, B.; Johnson, T. W.; Shelton, D.; Oh, S.-H.; Boreman, G. D.; Raschke, M. B. Optical Dielectric Function of Gold. *Phys. Rev. B* **2012**, *86* (23), 235147.

(37) Dossou, K. B.; Botten, L. C.; Asatryan, A. A.; Sturmberg, B. C. P.; Byrne, M. A.; Poulton, C. G.; McPhedran, R. C.; de Sterke, C. M. Modal Formulation for Diffraction by Absorbing Photonic Crystal Slabs. *J. Opt. Soc. Am. A* **2012**, *29* (5), 817–831.

(38) Huck, C.; Toma, A.; Neubrech, F.; Chirumamilla, M.; Vogt, J.; De Angelis, F.; Pucci, A. Gold Nanoantennas on a Pedestal for Plasmonic Enhancement in the Infrared. *ACS Photonics* **2015**, *2* (4), 497–505.

(39) Collin, S. Nanostructure Arrays in Free-Space: Optical Properties and Applications. *Rep. Prog. Phys.* **2014**, *77* (12), 126402.

(40) Mello, M. L. S.; Vidal, B. C. Changes in the Infrared Microspectroscopic Characteristics of DNA Caused by Cationic Elements, Different Base Richness and Single-Stranded Form. *PLOS ONE* **2012**, *7* (8), e43169.